An MRI-powered and controlled actuator technology for tetherless robotic interventions

Panagiotis Vartholomeos[1], Christos Bergeles[1], Lei Qin[2] and Pierre E. Dupont[1]

Abstract

This paper presents a novel actuation technology for robotically assisted MRI-guided interventional procedures. In the proposed approach, the MRI scanner is used to deliver power, estimate actuator state and perform closed-loop control. The actuators themselves are compact, inexpensive and wireless. Using needle driving as an example application, actuation principles and force production capabilities are examined. Actuator stability and performance are analyzed for the two cases of state estimation at the input versus the output of the actuator transmission. Closed-loop needle position control is achieved by interleaving imaging pulse sequences to estimate needle position (transmission output estimation) and propulsion pulse sequences to drive the actuator. A prototype needle driving robot is used to validate the proposed approach in a clinical MRI scanner.

1. Introduction

Magnetic resonance imaging (MRI) produces high-quality images without exposing the patient to ionizing radiation and also provides a single environment wherein surgical procedure planning, performance, and assessment can be conducted. These advantages are well recognized by the clinical and research communities, and have motivated research in robotically assisted magnetic resonance (MR)-guided interventions (Tsekos et al., 2007).

A variety of MR-compatible robotic systems have been designed. These systems are usually developed to treat a specific region of the body, such as the prostate, breast or brain, and most perform the task of needle insertion for either biopsies or interventional therapies (Masamune et al., 1995; Tsekos et al., 2005; Patriciu et al., 2007; Fischer et al., 2008; Li et al., 2011; Song et al., 2011).

Conventional actuation principles involving electromagnetic motors are generally not MR-compatible since they both interfere with the magnetic fields used for imaging and also are unsafe since they experience high forces and torques when placed inside the scanner bore. Therefore, alternative actuation principles are employed, such as ultrasonic motors, a technology which has been maturing over the last four decades (Barth, 1973). The first example of an MRI-safe ultrasonic-powered robot was the needle-insertion neurosurgical robot presented by Masamune et al. (1995). Since then, many successful MRI-safe robotic

systems have been introduced utilizing ultrasonic motors (Chinzei et al., 2000; Tsekos et al., 2005, 2007), one of the most recent examples being the needle-steering of Su et al. (2012), which employs non-harmonic piezoelectric actuators.

MR-compatibility measurements, however have demonstrated that ultrasonic motors can produce a large reduction in signal-to-noise ratio (SNR) when operated inside the MRI bore (Fischer et al., 2008). This issue can be overcome by turning off motor power during imaging, thus complicating the implementation of real-time control, or by placing ultrasonic motors at a distance from the bore. In the latter case, however, flexibility, backlash and friction are introduced due to remote actuation of joints (Tsekos et al., 2005). Recent results utilizing linear amplifiers and carefully shielded electronics suggest that simultaneous actuation and imaging is possible (Su et al., 2012) at the expense of increased system cost.

An alternative to ultrasonic powering is pneumatic actuation. Pneumatic actuators are MR-compatible and do not cause SNR reduction, but they do require a complicated

[1]Department of Cardiovascular Surgery, Boston Children's Hospital, Harvard Medical School, Boston, MA, USA
[2]Dana Farber Cancer Institute, Boston, MA, USA

Corresponding author:
Pierre E. Dupont, Department of Cardiovascular Surgery, Boston Children's Hospital, 300 Longwood Avenue, Boston, MA 02115, USA.
Email: pierre.dupont@childrens.harvard.edu

installation that involves locating a control unit, power supplies, amplifiers and valves external to the MRI shielded room (Patriciu et al., 2007; Li et al., 2011; Tokuda et al., 2012). Furthermore, the pneumatic transmission lines lower the bandwidth and, in combination with the spatial constraints of the MRI bore, complicate robot design (Song et al., 2011).

The contribution of this paper is to propose a new tetherless MR-compatible actuation technology in which the MRI scanner is programmed to deliver power, to estimate actuator state and to perform closed-loop control. The complete actuator system does not need any peripheral devices (amplifiers, drivers, pumps, etc.) inside or outside the MRI room. Control and sensing operations are accomplished using the MRI host computer, the MRI electronics and the gradient and radiofrequency (RF) coils.

Since the actuators leverage the existing MRI infrastructure, are completely self-contained and can be fabricated from inexpensive components, they offer a simple and potentially disposable alternative to existing technologies. In addition, since the MR system provides both imaging and control of the interventional procedure using a common software interface, the integration of actuation and imaging is simplified.

Actuation is based on one or more small ferromagnetic bodies safely contained inside the motor that serve to convert the electromagnetic energy of the MR gradients into mechanical energy. The ferromagnetic bodies have a small volume and can be designed to be outside the imaging region of interest, thus not affecting imaging quality. MRI gradients have been previously employed for actuation of ferromagnetic particles in the vasculature (Martel et al., 2007, 2009; Arcese et al., 2011). For example, closed-loop trajectory control of a 1.5 mm diameter ferromagnetic sphere in the carotid artery of a pig was demonstrated by Martel et al. (2007, 2009). In these papers, the ferromagnetic particle is itself the robot.

Inspired by this work, the current paper proposes a means to use the same force production principles to design actuators that can power more general interventional robots. In the next section, the background theory on the generation of actuator forces by the MRI scanner is presented. Section 3 describes the principle of actuation and, using a one-degree-of-freedom (1-DOF) needle-driving robot as a motivational example, provides guidelines for relating clinically desired needle insertion forces to actuator and transmission design parameters.

Section 4 compares the dynamic performance that can be achieved when estimating actuator state via motor rotor angle versus needle position. The former enables a nested controller structure in which an inner loop performs motor commutation (ensuring maximum output torque) while an outer loop performs needle position control. In contrast, while needle position estimation precludes commutator control (since the transmission amplifies needle position error), it is shown that open-loop commutation can be effective for the force profiles associated with needle tissue insertion. Consequently, this approach is employed in the remainder of the paper and a method for MRI-based needle position estimation is given in Section 5. Section 6 presents a prototype 1-DOF needle driving robot together with experiments validating the force capabilities of the actuator and demonstrating closed-loop control based on needle position estimation. Conclusions appear in the final section of the paper.

2. Background theory

When a ferromagnetic body is placed inside an MRI bore, it becomes magnetized due to the strong and uniform central field, $\vec{B}_0$, directed along the axis of symmetry of the bore. The magnetization across the volume of the body can be approximated as a lumped effect at the center of mass (CM) of the body (Abbott et al., 2007). Consequently, the magnetized body is approximated by a magnetic dipole placed at its CM. For typical central field strengths, the magnetization magnitude asymptotically approaches the saturation magnetization value $\vec{M}_s$ of the material, and its direction points along the easy magnetization axis of the body, which depends on the shape anisotropy of the material. The magnetic torque and force acting on the body can be computed using the expressions for the torque $\vec{T}$ and force $\vec{F}$ acting on a magnetic dipole in an external field $\vec{B} = \vec{B}_0 + \vec{B}_g$:

$$\vec{T} = V\vec{M}_s \times \vec{B} \qquad (1)$$
$$\vec{F} = V(\vec{M}_s \cdot \nabla)\vec{B} \qquad (2)$$

where $\vec{B}_g$ is the magnetic field generated by the gradient coils, V is the magnetic volume of the material and $\vec{M}_s$ is the saturated magnetization per unit volume of the material. The magnetic torque $\vec{T}$ tends to rotate the ferromagnetic body so that $\vec{M}_s$ aligns with the direction of the $\vec{B}_0$ field (the contribution of the $\vec{B}_g$ field to the torque $\vec{T}$ is negligible). Since the $\vec{B}_0$ field inside an MRI is fixed and cannot be controlled by the user, the torque $\vec{T}$ is not a valuable quantity for control purposes. The magnetic forces $\vec{F}$ depend on the spatial variation of the field $\vec{B}_g$, generated by the gradient coils. These comprise a pair of Maxwell coils and four pairs of saddle coils located orthogonal to each other as shown in Figure 1.

Resolving the force $\vec{F}$ of (2) in the *XYZ* frame that is attached to the isocenter of the bore (see Figure 1), yields

$$\left[\vec{F}_x \ \vec{F}_y \ \vec{F}_z \right] = VM_{sz} \left[\frac{\partial B_{gx}}{\partial z} \ \frac{\partial B_{gy}}{\partial z} \ \frac{\partial B_{gz}}{\partial z} \right] \qquad (3)$$

where it has been reasonably assumed that $M_{sx}, M_{sy} \ll M_{sz}$. Equation (3) shows that the MRI forces acting on a ferromagnetic body are related to the three orthogonal gradients. The gradient coils are designed to generate (for imaging purposes) the three linearly independent gradients given by

$$\vec{g} = [g_x \ g_y \ g_z] = \left[\frac{\partial B_{gz}}{\partial x} \ \frac{\partial B_{gz}}{\partial y} \ \frac{\partial B_{gz}}{\partial z} \right] \qquad (4)$$
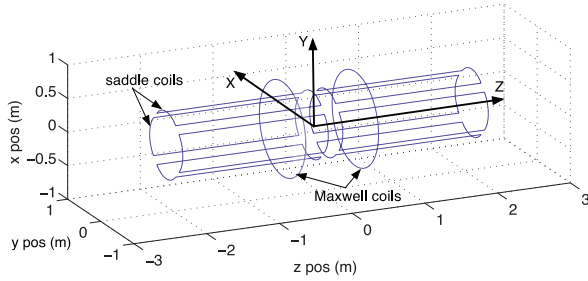
Fig. 1. MRI gradient coils configuration. The *z*-axis gradient is generated by a pair of Maxwell coils. The *x* and *y* gradients are generated by four pairs of saddle coils.

The Maxwell equations state that field lines must form closed loops, however, i.e. $\nabla \cdot \vec{B} = 0$, and also that they must exhibit zero curl, i.e. $\nabla \times \vec{B} = 0$, at any point outside the coil conductors. This implies that it is impossible to generate the gradients in (4) without also generating concomitant gradients. As a result, the complete field $\vec{B}_g$ is given by (Han et al., 2008)

$$\vec{B}_g(\vec{x}) = (\vec{g} \cdot \vec{x})\hat{z} + \mathbf{G}_c \vec{x} \qquad (5)$$

where $\vec{g}$ is as given in (4), $\vec{x}$ is the position vector from the origin if the *XYZ* frame, $\hat{z}$ is the unit vector along the *z*-axis and $\mathbf{G}_c$ is a matrix containing the concomitant gradients and is given by

$$\mathbf{G}_c = \begin{bmatrix} -g_z/2 & 0 & g_z \\ 0 & -g_z/2 & g_y \\ 0 & 0 & 0 \end{bmatrix} \qquad (6)$$

Differentiating the *x* and *y* components of Equation (5) with respect to the *z* coordinate yields

$$\left[\frac{\partial B_{gx}}{\partial z}\right] = \left[\frac{\partial B_{gz}}{\partial x}\right], \quad \left[\frac{\partial B_{gy}}{\partial z}\right] = \left[\frac{\partial B_{gz}}{\partial y}\right] \qquad (7)$$

Hence, the gradients of (3) are equal to the imaging gradients of (4) and, furthermore, all three are linearly independent. Thus they are capable of inducing 3-DOF motion in a ferromagnetic body.

3. Actuator design

The proposed actuator is comparable to an electric motor. It consists of the stator, which, in this case, is composed of the MRI scanner together with the stationary components of the actuator, and a rotor, which is the rotating portion of the actuator that contains the ferromagnetic material. As depicted in Figure 2, the rotor consists of a ferromagnetic object enclosed in a cavity in a lever arm that rotates at a fixed distance about an axis.

The object is contained in a cavity rather than embedded in the lever arm since, by (1), a large torque would be generated if rotation of the lever arm caused the magnetization vector of the sphere to rotate out of alignment
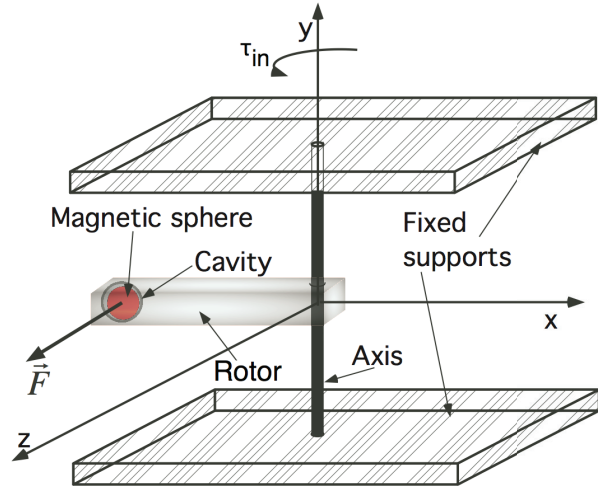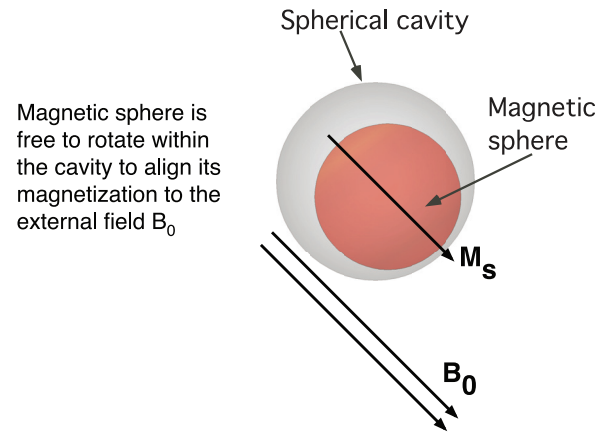

Fig. 2. Actuator schematic.

Fig. 3. Ferromagnetic sphere rolls and slides inside the cavity to maintain alignment of its magnetic axis with the B_0 field of the scanner.

with the B_0 field. Except in the case that the actuator axis was perfectly aligned with the central axis, such a torque would stall the actuator. Therefore, the ferromagnetic body must be free to rotate within its cavity. To minimize friction between the ferromagnetic body and cavity walls, the geometry of the ferromagnetic body should be selected as spherical and the surfaces of the sphere and cavity should be designed to minimize friction.

Rotation of the actuator is generated by applying magnetic field gradients to generate a force $\vec{F}$ on the ferromagnetic sphere as shown in Figure 2. Assuming for simplicity that the (*xyz*) frame of the actuator coincides with the (*XYZ*) frame of the isocenter of the MRI bore (Figure 1), gravity is directed along the *y*-axis and so does not affect rotor motion. From the free-body diagram of Figure 4, the single-DOF motion is described by the following scalar equation

$$J\ddot{\theta} = -b\dot{\theta} - T_{\mathrm{fr}} - T_l + r_1 F \sin(\phi - \theta) \qquad (8)$$
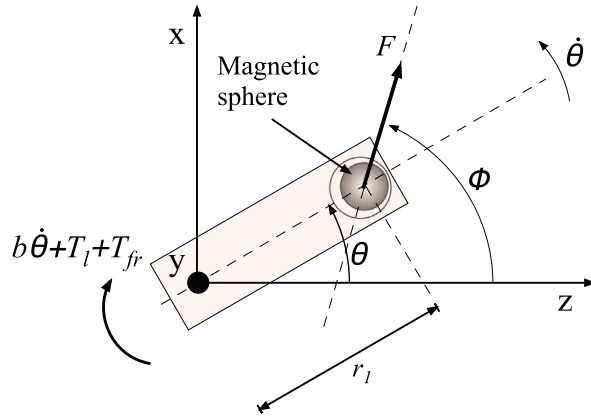
Fig. 4. Rotor coordinate frame and variables.

in which J is the moment of inertia of the composite body that comprises the axis, the lever and the sphere, r_1 is as shown in Figure 4, b is the coefficient of viscous friction and θ is the angle of the rotor. The term T_{fr} is the summation of all non-viscous friction terms as seen by the input including the friction component contributed by the ferromagnetic sphere when it slides inside the cavity. Also, T_l is the load torque and ϕ is the angle of the magnetic gradient. It is reasonably assumed that the eddy currents induced on the millimeter-scale chrome steel sphere are very small and can be neglected (Giffin et al., 2010).

The angle θ is called the *mechanical angle* and the angle ϕ is called the *magnetic angle*. Their difference is called the *slip angle*, ψ,

$$\psi = \phi - \theta. \qquad (9)$$

Note that actuator torque is maximized when $\psi = \pi/2$. The values of $\vec{F}$ and ϕ are given by

$$\|\vec{F}\| = \sqrt{F_x^2 + F_y^2 + F_z^2}, \quad \phi = \tan^{-1}(F_x/F_z) \qquad (10)$$

where F_x, F_y, F_z are as given in (2).

3.1. Needle driving

To examine the potential of this technology for robotically assisted MRI-guided procedures, it is considered here in the context of needle insertion: specifically considering the forces needed to drive a needle into tissue. For this application, rotary actuator motion must be converted into linear needle motion using transmission elements. The type of transmission elements employed as well as the overall transmission ratio are design choices. As an illustrative example, Figure 5 depicts one possible design, utilized later in the paper, employing a gear train together with a rack and pinion. To maximize output force, the x–z plane of the rotor is selected to coincide with the X–Z plane of the MRI bore. Otherwise, part of the magnetic force must compensate for gravity. If the output force has to be applied at an angle with respect to the x–y plane, then bevel gears can be used to change the axis of rotation.

For the depicted transmission, the three gear ratios, G_1, G_2, G_3, are given by

$$G_1 = \frac{N_2}{N_1}, \quad G_2 = \frac{N_4}{N_3}, \quad G_3 = \frac{N_6}{N_5} \qquad (11)$$

in which N_i, $i = 1, \ldots, 6$, are the numbers of gear teeth. The reduction ratio between $\dot{\theta}$ and the rack speed u_r is then computed as

$$R = \frac{u_r}{\dot{\theta}} = \frac{r_2}{G_1 G_2 G_3} \qquad (12)$$

in which r_2 is the radius of the N_7 pinion.

Independent of the type of transmission, the important design variables are its transmission ratio, R, and its efficiency, η. To design an actuator to produce a desired needle force, F_n, the design equation is given by

$$F_n \leq \eta \frac{r_1 F}{R} = \eta \frac{r_1}{R} V M_{sz} \left. \frac{\partial B_g}{\partial z} \right|_{\text{max}} \qquad (13)$$

The force necessary to insert a needle varies with needle size and design as well as tissue type. Furthermore, the force can vary considerably during insertion with maxima occurring during puncture of elastic tissue layers. A number of papers have reported *in vivo* measurements of maximum needle forces. For example, Washio and Chinzei (2004) reported maximum forces of about 0.5 N inserting a 2 mm diameter needle into porcine spleen. Maurin et al. (2004) reported maximum forces for manual 18G needle insertion in pigs of 0.7 N for liver, 0.74 N for kidney and 0.83 N for pancreas. Percutaneous insertion forces are higher; the same authors reported maximum forces for percutaneous liver insertion to be 3.73 N when performed manually and 1.89 N when performed robotically. Maximum forces for *in vivo* human prostate capsule puncture during brachytherapy have been reported to be about 8.9 N using 18G needles and 15.6 N for 17G needles (Podder et al., 2006).

Equation (13) provides the means to determine whether or not the proposed technology can produce clinically relevant forces. Table 1 presents two potential designs computed using (13) that span the range of reported maximum force data. These designs assume the standard maximum clinical MRI gradient of 40 mT/m and utilize a single chrome steel sphere. For simplicity, both designs employ a gear ratio, $G_1 G_2 G_3 = 125$ and a rotor radius of $r_2 = 18$ mm. Design 1, corresponding to the prototype presented in Section 6, is intended to produce maximum forces of 0.55 N (> 0.5 N), sufficient for porcine spleen insertion. Design 2 specifies a maximum force of 20 N, which would be sufficient for human prostate capsule puncture.

The factor of 40 difference in output force between these designs is achieved by varying three of the design parameters. First, the transmission efficiency is increased by a factor of 2.5 from the low initial value of 0.2 that is characteristic of low-precision components to the very conservative value of 0.5 which can be easily exceeded using high-precision transmission elements. Doubling the pinion
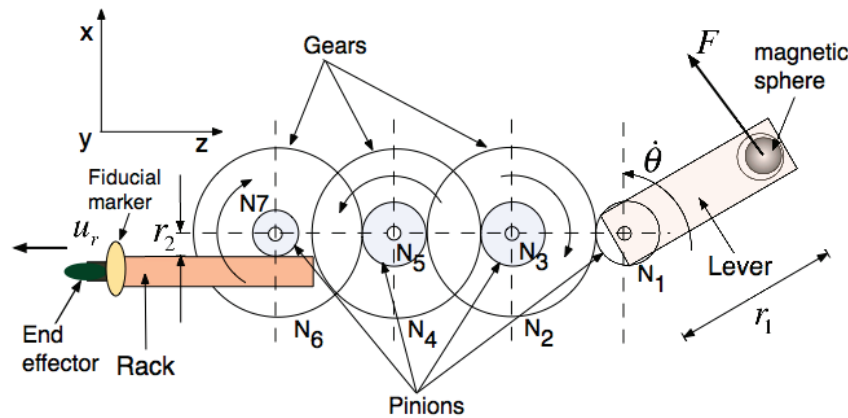
Fig. 5. Transmission unit incorporating gear train and rack and pinion elements.

Table 1. Design scenario parameters for producing clinically relevant forces.

	Parameter	Value
Common	Saturated magnetization, M_s [A m^{-1}]	1.36×10^6
Parameters	Maximum MRI gradient [mT/m]	40
	Gear ratio, $G_1 G_2 G_3$	125
	Rotor radius, r_1 [mm]	18
Design 1	**Desired force, F_n [N]**	**0.5**
	Efficiency [η]	0.2
	Pinion radius, r_2 [mm]	5
	Ferromagnetic sphere radius [mm]	3
Design 2	**Desired force, F_n [N]**	**20**
	Efficiency [η]	0.5
	Pinion radius, r_2 [mm]	10
	Ferromagnetic sphere radius [mm]	6

radius to 1 cm keeps the overall transmission size small while doubling the transmission ratio. Finally, doubling the ball radius to 6 mm provides a factor of 8 increase in volume and force.

While both designs utilized the current maximum gradient value of clinical scanners, 40 mT/m, it is interesting to note that higher gradients may become available in the pursuit of increased imaging resolution. For example, *in vivo* brain measurements using 300 mT/m gradients produced by 55 cm diameter gradient coils have recently been demonstrated (McNab et al., 2012). Such systems would enable an order of magnitude increase in actuator forces or, alternately, a reduction in transmission ratio and size.

3.2. MRI compatibility

Since the actuator technology utilizes magnetic gradients to produce propulsive forces on ferromagnetic material located within the actuator, it is necessary to ensure that the resulting actuators are MRI compatible. MRI compatibility typically involves satisfying three types of constraints: (1) maintaining image quality, (2) ensuring safety and (3) meeting geometric constraints. In the proposed approach, there is an additional constraint: (4) imaging

pulse sequences should not produce unintentional actuator motions or forces.

The first constraint implies that insertion and, ideally, operation of the actuator inside the scanner should not decrease image SNR in the imaging region of interest. This constraint is met in the proposed approach by placing the ferromagnetic material at a sufficient distance from the imaging region and by proper selection of actuator structural components, e.g. plastics.

To ensure the safety of the patient, medical personnel and the scanner, any ferromagnetic material used in an actuator should be constrained so as avoid any risk of creating an uncontrolled motion of the ferrous material itself or of the actuator, e.g. projectile motion. This is accomplished by sealing the ferrous material in a cavity so that it cannot escape the actuator and by properly fixing the actuator with respect to the scanner and the patient.

The geometric constraints of MRI compatibility relate to ensuring that the size of the actuator/robot does not create physical interference with either the patient or the scanner. While the proposed actuators do require mechanical transmissions to amplify output forces and torques, overall size remains modest. For example, the prototype needle driving robot presented later in the paper is sufficiently small to be

placed inside the scanner bore at any desired location on a patient's body.

Employing electromagnetic actuation introduces a new compatibility requirement in that the imaging sequences employed during actuation should not cause unintended actuator motions or forces. This can be achieved by developing imaging pulse sequences using gradient pulse magnitudes and/or directions that are non-propulsive. Alternately, the pulse sequence may be *balanced* such that it has no net propulsive effect. These techniques are utilized in the actuator state estimation of Section 5.

4. Dynamic behavior for open- and closed-loop control of slip angle

The position control loop for needle driving can be closed using MRI-based sensing of actuator position. Position sensing can either be achieved at the transmission output (needle position) or at the input of the transmission (rotor angle). Directly sensing needle position is desirable since it is the clinical quantity of interest and avoids any risk of insertion errors arising from image-based miscounting of rotor revolutions. MRI image-based tracking is also simpler than rotor tracking owing to its linear motion and lower velocity.

A disadvantage of needle position sensing, however, is that it does not provide an accurate estimate of rotor angle owing to the transmission ratio. Estimation of rotor angle can be important since production of maximum actuator torque depends on directing the magnetic gradient perpendicular to the rotor, i.e., regulating slip angle to $\psi = \pi/2$. In electric motors, this is referred to as commutation and is accomplished either mechanically (brushed motors) or electronically by closing a feedback loop around rotor angle. Thus, needle position control theoretically requires both an inner commutation loop to control slip angle and an outer loop to control needle position.

While MRI-based commutation control is both feasible and desirable in some circumstances (Bergeles et al., 2013), open-loop slip angle control can be sufficient in some applications. To understand the differences, this section compares closed-loop and open-loop control of slip angle. It is shown that open-loop slip angle control can be stable for needle-loading scenarios similar to those experienced during tissue insertion. Furthermore, the magnitude of applied needle forces can approach that of closed-loop control. For these analyses, Equation (8) is rewritten in terms of needle force, F_n as

$$J\ddot{\theta} = -b\dot{\theta} - T_{fr} - RF_n + r_1 F \sin(\phi - \theta) \quad (14)$$

$$u_r = R\dot{\theta} \quad (15)$$

Here, R and u_r are defined in (12). The terms J and b are the summation of the inertia and viscous friction terms, respectively, of all transmission stages as seen by the input of the system. All other terms are as defined above.

4.1. Closed-loop control of slip angle (commutation control)

During commutation control, slip angle is regulated to $\psi = \pi/2$. In this case, the steady-state output linear velocity u_r is given by

$$u_r = -\frac{R^2}{b}F_n + R\left(\frac{r_1 F}{b} - \frac{T_{fr}}{b}\right)$$
$$= -\frac{R^2}{b}F_n + R\left(\frac{r_1 VM_s B_{grad}}{b} - \frac{T_{fr}}{b}\right) \quad (16)$$

where

$$B_{grad} = \sqrt{\left(\frac{\partial B_{gz}}{\partial z}\right)^2 + \left(\frac{\partial B_{gx}}{\partial z}\right)^2} \quad (17)$$

Equation (16) reveals that under commutation control, the output velocity u_r is linearly related to the output force F_n through a negative proportionality constant. The maximum permissible output load (stall or blocking force) is obtained for $u_r = 0\,\mathrm{ms}^{-1}$ and is given by:

$$F_n^{max} = (r_1 F - T_{fr})/R \quad (18)$$

Setting the output force F_n to zero yields the maximum output velocity u_r^{max}. This maximum output velocity corresponds to a maximum rotational velocity of the lever $\dot{\theta}^{max} = u_r^{max}/R$, which in turn gives the maximum gradient frequency ω^{max} for a given B_{grad}:

$$\omega^{max} = (r_1 F - T_{fr})/b \quad (19)$$

4.2. Open-loop control of slip angle

The preceding subsection requires a nested control structure in which an inner control loop regulates slip angle while an outer loop controls actuator position or velocity. This subsection addresses the simpler case (from an implementation perspective) in which slip angle is not controlled. To understand whether this approach may suffice for some interventional applications, this subsection assesses stability for two important cases. The first is when a constant load is applied to an actuator that is driven at constant velocity. The second case corresponds to a linear elastic load driven at constant velocity. This latter case is comparable to the loading experienced by a needle pressing against tissue prior to puncture. In both cases the MRI scanner is programmed to generate gradients rotating in the X–Z plane at constant frequency ω. The gradients are given by

$$\left[\frac{\partial B_{gx}}{\partial z} \quad \frac{\partial B_{gz}}{\partial z}\right] = B_{grad}[\cos \omega t \quad \sin \omega t] \quad (20)$$

4.2.1. Constant-velocity constant-load stability In the open-loop case, stable operation of the actuator implies the rotor synchronizes with the rotating gradient frequency, ω. To analyze the steady-state behavior of the system in

response to the gradients of (20), the system (14) is rewritten in terms of the slip angle, $\psi = \phi - \theta$, in which $\phi = \omega t$. Time is also non-dimensionalized to reduce the number of free parameters using the non-dimensionalized time τ:

$$\tau = \sqrt{\frac{r_1 F}{J}} t \qquad (21)$$

The resulting equation is given by

$$\ddot{\psi} + \alpha \dot{\psi} + \sin \psi = \beta \qquad (22)$$

where $\dot{\psi}$ and $\ddot{\psi}$ are now differentiated with respect to τ and

$$\alpha = \frac{b}{\sqrt{r_1 F J}} \qquad (23)$$

$$\beta = (RF_n + b\omega + T_{\text{fr}})/r_1 F \qquad (24)$$

Insight into the behavior of the rotor can be gained by observing that (22) is the equation of a damped pendulum experiencing a constant applied torque and that slip angle ψ corresponds to the angle of the pendulum. Thus, it can be anticipated that the system will possess one stable and one unstable equilibrium point at $\psi = \{0, \pi\}$, respectively, when the applied torque $\beta = 0$. Referring back to Figure 4, these configurations correspond to the rotor being aligned and anti-aligned, respectively, with the direction of the rotating magnetic force, F. For a non-zero applied torque β, these equilibria will shift such that the torque generated on the rotor by F balances β. This reasoning is demonstrated in the analysis below.

4.2.1.1. Determination of equilibrium points Expressing (22) in state-space form with $x_1 = \psi$ and $x_2 = \dot{\psi}$ yields

$$\dot{x}_1 = x_2 \qquad (25)$$
$$\dot{x}_2 = -\alpha x_2 - \sin x_1 + \beta$$

The equilibrium points of the states (x_1, x_2) are $(\psi^*, 0)$ and satisfy

$$\dot{x}_1 = \dot{x}_2 = 0 \qquad (26)$$

and, as expected, are given by

$$\psi^* = \sin^{-1} \beta \qquad (27)$$

The condition, $|\beta| \leq 1$, for existence of a solution can be seen from (24) to require that the total torque arising from friction and the applied load not exceed the maximum magnetic torque produced by the magnetic force F acting over the rotor moment arm radius of r_1.

Equation (27) yields two isolated equilibrium points $\{\psi_1^*, \psi_2^*\}$, in the range $[-\pi, \pi]$, as given below:

$$\psi_1^* = \sin^{-1} \beta, \quad |\psi_1^*| \leq \pi/2 \qquad (28)$$
$$\psi_2^* = \pi - \psi_1^*, \quad |\psi_2^*| \geq \pi/2 \qquad (29)$$

4.2.1.2. Stability analysis of the equilibrium points Linearizing (26) about the equilibrium points yields the error equation

$$\dot{e} = Ae, \quad e = \left[\psi - \psi^*, \ \dot{\psi} - 0\right]^{\text{T}} \qquad (30)$$

where the stability matrix A is given by

$$A = \begin{bmatrix} 0 & 1 \\ -\cos \psi^* & -\alpha \end{bmatrix} \qquad (31)$$

The eigenvalues $\lambda_{1,2}$ of matrix A are given by

$$\lambda_{1,2} = \frac{-\alpha \pm \sqrt{\alpha^2 - 4 \cos \psi^*}}{2} \qquad (32)$$

Thus, an equilibrium value ψ^* is locally asymptotically stable for $|\psi^*| < \pi/2$, locally marginally stable for $\psi^* = \pi/2$ and locally unstable for $|\psi^*| > \pi/2$. Hence, for the realistic case of $\alpha > 0$, the equilibrium ψ_1^* in (28) is asymptotically stable and ψ_2^* in (29) is unstable.

Figure 6 illustrates the pendulum analogy in the context of the actual system. The magnetic gradient, rotating with angular velocity ω, is depicted at the instant in which it is directed along the z-axis such that the magnetic angle $\phi = 0$ and the rotor angle $\theta = -\psi$. In this snapshot view, the magnetic gradient is analogous to gravity acting on a pendulum which also experiences an opposing constant load torque of magnitude $r_1 F \beta$. The magnetic and load torques balance at the rotor configurations ψ_1^* and ψ_2^*, which are arranged symmetrically with respect to the x-axis. As the load torque increases, the equilibria move toward the negative x-axis where they coalesce at $\psi_1^* = \psi_2^* = \pi/2$, the configuration at which magnetic torque is a maximum. This also corresponds to the configuration at which ψ_1^* becomes unstable. Thus, stability can only be maintained for load torques that are less than the maximum magnetic torque.

4.2.1.3. Domain of attraction of equilibrium points It is important to understand how far the region of stability extends around the stable equilibrium point ψ_1^*. For example, such an analysis will reveal whether stable rotation will result if the rotor is started from rest or a perturbation in applied force drives the system from the equilibrium point. Since (25) is second order and autonomous, the domain of attraction can be geometrically represented in the phase plane. Figure 7 illustrates the stable and unstable regions for three sets of (α, β) values, namely: $\{(\alpha_1, \beta_1) = (0.96, 0)\}$, $\{(\alpha_2, \beta_2) = (91.1, 0.0096)\}$, $\{(\alpha_3, \beta_3) = (169.2, 0.018)\}$. For each value, the separatrix, bounding the stable state initial conditions in its interior, is labeled. Outside each separatrix, the system is unstable and undergoes complete rotations, i.e. the rotor does not follow the magnetic gradient. Note that increasing the viscous damping shifts the slip angle equilibrium point ψ_1^*, as given by (28), to the right and also reduces the size of the domain of attraction.
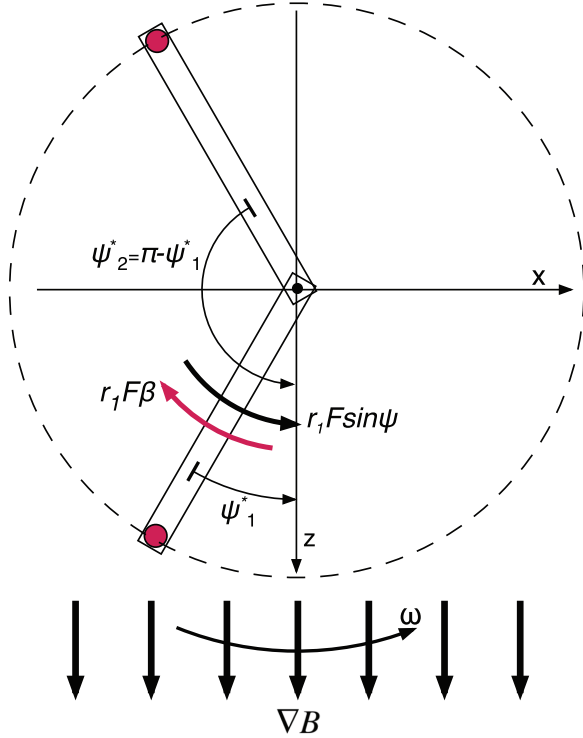
Fig. 6. Rotor equilibrium configurations for a rotating magnetic gradient depicted at the instant when magnetic angle $\phi = 0$ so that rotor angle $\theta = -\psi$.
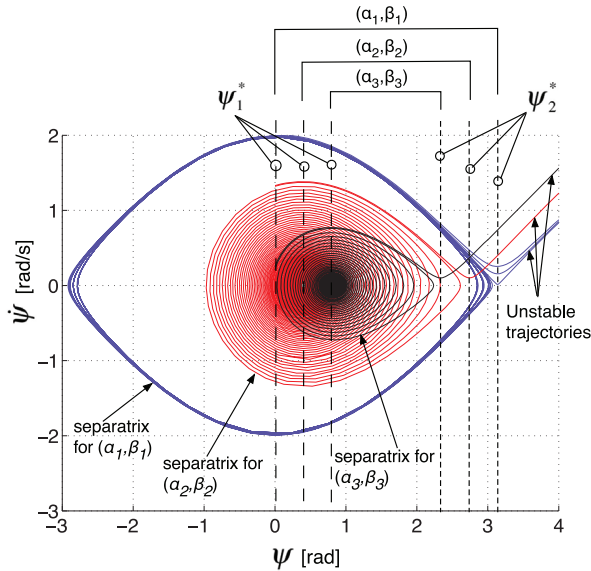

Fig. 7. Phase portrait of the slip angle rate, $\dot{\psi}$, versus slip angle, ψ, for system (25) for three sets of (α, β).

For experimental evaluation, it is of interest to predict the maximum angular gradient velocity ω in (20) that will result in stable rotor rotation when the rotor is started from rest. Assuming that the rotor angle is initialized at the slip angle equilibrium value, this value is given by the maximum slip angle rate achieved on the separatrix. For the undamped

case, $\alpha = 0$, an analytical expression can be derived using the impulse momentum principle, i.e. by relating the kinetic energy of the system when $\psi = \psi_1^*$ to the potential energy of the system at $\psi = \psi_2^*$ through the work done by the load torque,

$$E\left(\psi_1^*, \sqrt{\frac{J}{r_1 F}}\omega_{\max}\right) + W(\beta) = E(\psi_2^*, 0)$$

$$\frac{1}{2}\frac{J}{r_1 F}\omega_{\max}^2 + \int_{\psi_1^*}^{\psi_2^*}\beta\,dx_1 = \int_{\psi_1^*}^{\psi_2^*}\sin x_1\,dx_1$$

$$\frac{1}{2}\frac{J}{r_1 F}\omega_{\max}^2 + \beta(\psi_2^* - \psi_1^*) = \cos\psi_1 - \cos\psi_2 \quad (33)$$

$$\omega_{\max} = \sqrt{\frac{r_1 F}{J}}\sqrt{2(\cos\psi_1^* - \cos\psi_2^* - \beta(\psi_2^* - \psi_1^*))} \quad (34)$$

where the time scaling factor of (21) has been employed to compute angular velocity. The physical interpretation is that whenever the relative velocity between the rotor and the magnetic gradient exceeds the value $\dot{\psi} = \omega_{\max}$ the rotor becomes unstable and stalls.

4.2.2. Constant-velocity elastic-load stability

During needle insertions, large forces are typically required to puncture tissue layers, however, the load applied to the needle prior to puncture is not constant, but rather is viscoelastic. As an approximation to the viscoelastic tissue deformation force prior to puncture, this subsection considers the effect of an elastic load on the stability of the actuator during constant velocity operation.

In this case, the MRI gradients are as given in Equation (20). The actuator rotor synchronizes to the constant gradient frequency and the rack pushes at a constant speed against the elastic material. The load force is given by

$$F_n = kl \implies F_n = kRx_1 \quad (35)$$

where k is the tissue stiffness constant, and l is the deformation of the elastic load. Equation (26) is rewritten as

$$\dot{x}_1 = x_2 \quad (36)$$
$$\dot{x}_2 = -\alpha x_2 - \sin x_1 - \gamma x_1 + \beta \quad (37)$$

where

$$\gamma = \frac{kR^2}{r_1 F} \quad (38)$$

$$\beta = \frac{b}{\sqrt{Jr_1 F}}\omega + \frac{T_f}{r_1 F} + \frac{kR^2\sqrt{J}}{\sqrt{(r_1 F)^3}}\omega\tau \quad (39)$$

For this case, we can derive a time-dependent equilibrium trajectory for slip angle ψ^* as

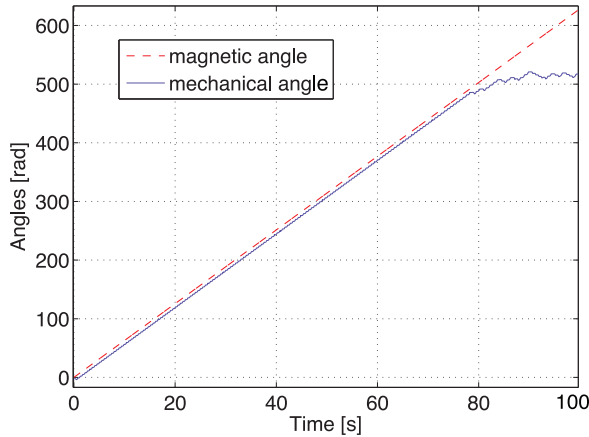$$\psi^* = \sin^{-1}\left(\gamma\omega\tau\sqrt{\frac{J}{r_1 F}} + \beta + \alpha\omega\right) \quad (40)$$

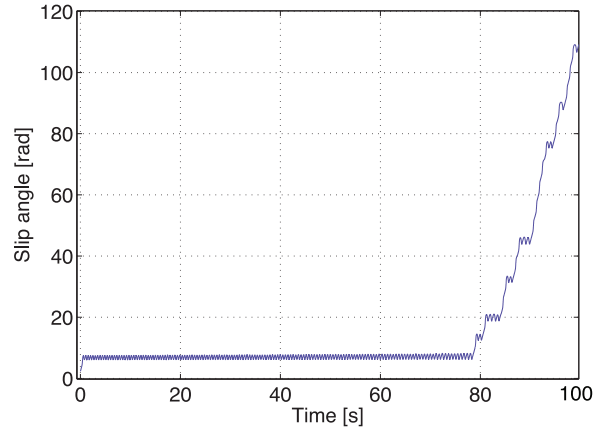**Fig. 8.** Simulation of constant-velocity elastic-load response: rotor angle, θ, and magnetic angle, ϕ, versus time.

and the corresponding matrix **A** of the linearized system is given by

$$A = \begin{bmatrix} 0 & 1 \\ -\cos\psi^* & -\alpha \end{bmatrix} \qquad (41)$$

Since the magnetic torque is bounded, it can be anticipated that the system response will be stable for small load torques, but will become unstable as this limit is approached. Simulation was used to examine the transient response and transition to instability of this time-varying system in response to increasing load torque. To obtain qualitative results, the parameter values for Design 1 in Table 1 were used. In the place of efficiency, the friction parameter values of $T_{\mathrm{fr}} = 7.0 \times 10^{-5}$ Nm and $b = 1.0 \times 10^{-7}$ Nms/rad were used.

Figure 8 shows the evolution of rotor angle and magnetic angle over time, up to the point of instability. Figures 9 and 10 illustrate how the slip angle ψ oscillates about the equilibrium value $\psi_1^*(t)$. As the force increases, $\psi_1^*(t) \to \pi/2$, the system becomes unstable and the rotor stalls. As can be seen in Figure 11, at the point of instability the output force is maximized.

These results indicate that open-loop control of the slip angle can be effective in loading scenarios similar to those of needle insertion. This indicates that closed-loop control of needle position can be accomplished with a single control loop that utilizes measurements of needle position (actuator position at the output of the transmission). An MRI-based method for estimating needle position is described in the next section.

5. MRI-based needle position sensing and closed-loop control

A variety of MRI-based needle tracking methods are possible. The most straightforward approach for needle interventions is to segment and track the needle in the MR image (Lewin, 1999). Alternatively, fiducial markers can be employed (van der Weide et al., 2001; Busse et al., 2007)
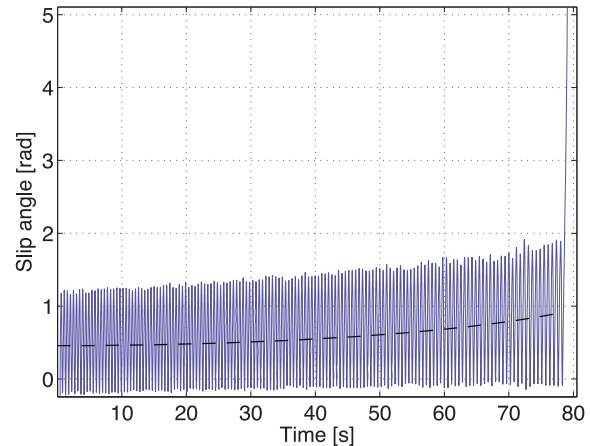

Fig. 9. Simulation of constant-velocity elastic-load response: slip angle, ψ, versus time.

Fig. 10. Expanded scale view of slip angle showing average (dashed) and oscillations leading up to instability.
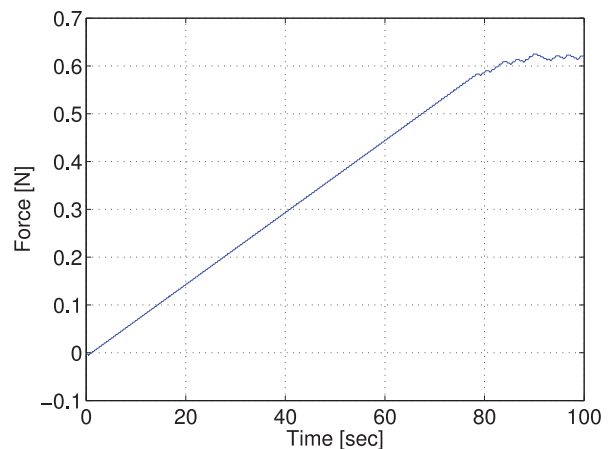

Fig. 11. Output force applied to elastic load versus time.

or the propulsive ferromagnetic material itself can be used as a fiducial marker (Felfoul et al., 2008). A third approach employs miniature receiving coils tuned to the RF of the MRI scanner (Qin et al., 2013). This approach, however,
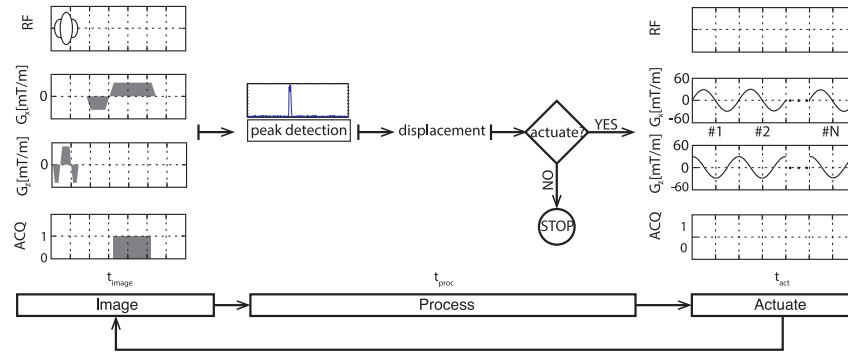
Fig. 12. Controller pulse sequence consisting of interleaved imaging and propulsion pulse sequences.

requires running a cable into the scanner bore and is not considered here since the focus of this paper is on tetherless robots.

There are several challenges to combining tetherless MRI-based actuation and sensing. First, this approach requires the interleaving of imaging and propulsion pulse sequences, which means that propulsion forces are only applied during a portion of each control cycle. Consequently, imaging sequences should be designed to be as fast as possible. Second, they should be designed to produce no net propulsive effect. With respect to the first criteria, imaging using standard pulse sequences is unacceptably slow. For example, as reported by Moche et al. (2008), one of the fastest imaging sequences, TrueFISP, creates an image in 0.4 s.

In the context of millimeter-scale robots propelled through the bloodstream, both criteria have been considered by Felfoul et al. (2008) and Chanu et al. (2008) where the signature of the ferromagnetic material of the robot produced in the surrounding tissue was used for tracking. Unfortunately, this approach cannot be directly applied to the actuator of Figure 5 as the ferromagnetic material of the rotor does not generate a magnetic signature since it is not surrounded by tissue or water and consequently is invisible in the MR image.

As an alternative approach, image-based tracking of a fiducial marker attached to the rack, as shown in Figure 5, is employed. Employing a fiducial marker outside the tissue enables the use of fast single-dimensional projections based on a gradient-echo pulse sequence as exploited by Chanu et al. (2008) and Zhang et al. (2010) since the marker is the only MRI-visible object in the *xy* plane over a range of values along the *x*-axis exterior to the tissue being penetrated.

As described in the next section, this technique resulted in an imaging pulse sequence duration of 12 ms. In this sequence, the gradients were applied over only a fraction of this time and were also balanced (see Figure 12) such that positive and negative pulses were largely offsetting. Furthermore, imaging gradient magnitudes were significantly smaller than actuation magnitudes. Consequently,

this approach to MRI-based position sensing provides the speed and non-propulsive properties needed for closed-loop position control.

As shown in Figure 13, marker position can be estimated from the single-dimensional gradient echo projections using peak detection or correlation. These simple approaches do not work in the presence of nearby tissue, however, since the tissue signal distorts the single-dimensional marker projection. Robust needle tracking can be accomplished, though, through use of a background suppression algorithm (Bergeles et al., 2012). In this approach, the single-dimensional tissue projection is first recorded prior to the introduction of the fiducial marker into the scanner. During tracking, this background signal, termed K, is removed from the recorded single-dimensional projection, by means of

$$ S' = \frac{S}{K + \epsilon} \tag{42} $$

in which S and S' are the original and amplified single-dimensional projections, respectively, and $\epsilon = 0.1$ is a small constant to avoid division by zero. Direct background subtraction (i.e. $S' = |S - K|$) is inapplicable because the background signal varies between tracking cycles and S' yields false peaks.

5.1. Closed-loop needle position control

In needle positioning, it can be problematic to overshoot or oscillate around the goal configuration. Consequently, the controller is designed to advance unidirectionally until the difference between the desired and estimated displacement is less than the control cycle displacement. The control cycle as shown in Figure 12 consists of a single gradient projection along the *z*-axis for needle tracking. The controller compares the needle position estimate with the desired value and either stops or executes a series of sinusoidal propulsive sequences. The number of propulsive sinusoids applied between tracking sequences can be selected, for example, to correspond to the minimum observable needle displacement.
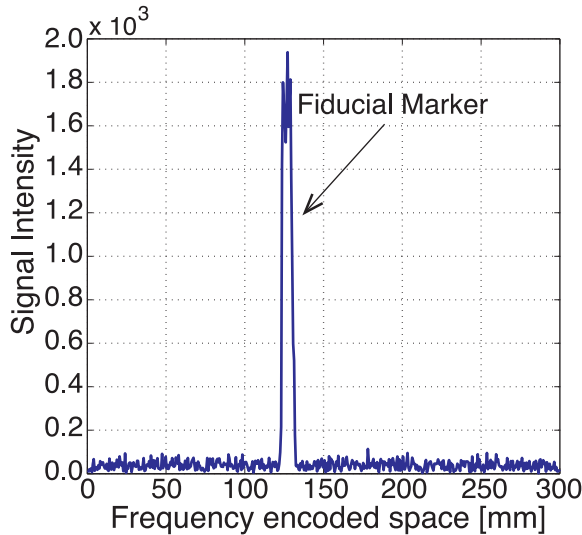
Fig. 13. Fiducial marker position estimation using *x*-axis projections. The plot shows signal intensity versus position in the absence of tissue.

6. Experiments

A prototype actuator was constructed to experimentally evaluate the concepts proposed in the preceding sections. Goals included demonstrating the capability to design for clinically relevant needle insertion forces, validating the stability and force production potential of open-loop slip control, and demonstrating closed-loop needle position control using interleaved pulse sequences to perform needle tracking and actuation.

The prototype, shown in Figure 14, was constructed to achieve an output force of 0.5 N using the parameters of Design 1 in Table 1. It was constructed using LEGO® parts since these plastic components are MRI compatible and enable efficient testing of alternate designs. Given the high component tolerances and friction, however, the transmission efficiency was anticipated to be low in accordance with the design parameter of $\eta = 0.2$.

With overall dimensions of 10 cm × 10 cm × 6 cm, the device is small enough to be positioned at a variety of locations on a patient inside the scanner bore. As shown in Figure 14, a 3 mm radius chrome steel ball bearing was safely enclosed in a cavity on the rotor arm. Needle stroke is determined by the length of the rack component, which for the tests performed here was 2.5 cm. The fiducial marker used for needle position estimation is an MR-SPOTS marker (Beekley Medical, CT). For those experiments involving needle insertion, MRI-compatible biopsy needles were used. To evaluate MRI image quality of the assembled system, measurements of the SNR were made by placing the MRI-powered actuator next to a porcine heart and it was demonstrated that no SNR deterioration occurred.

Three sets of experiments were conducted. The goal of the first set was to determine whether needle insertion under
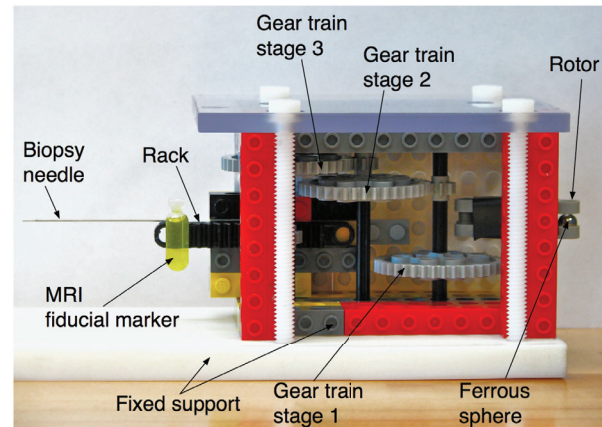

Fig. 14. Actuator prototype with biopsy needle and marker.

open-loop control of slip angle using the prototype actuator was possible. For these experiments, multiple insertion trials were conducted into porcine hearts. The magnetic gradient was rotated at a constant frequency for a sufficient time duration to produce epicardial puncture and subsequent needle insertion. The direction of rotation was then reversed such that the needle was withdrawn from the tissue. These experiments demonstrated successful needle insertion and removal. A video of one insertion appears as multimedia Extension 1. The MRI scanner can be heard in the video soundtrack.

Based on these results, a second set of experiments was performed to provide a detailed evaluation of open-loop slip angle control and assessment of maximum force output under conditions of constant input velocity and an elastic needle load as described in Section 4.2.2. A third set of experiments was then conducted to evaluate marker-based needle tracking and interleaved imaging and actuation to perform closed-loop needle positioning as described in Section 5. All experiments were conducted in a clinical GE 1.5 T MRI scanner (Milwaukee, WI) with pulse sequences programmed using the EPIC API.

6.1. Constant-velocity elastic-load experiments

A series of experiments were conducted to verify the properties of open-loop slip angle control in terms of maximum force output and stability of rotor motion. In these experiments, the magnetic gradient direction was rotated at constant frequency in the horizontal plane causing the rack to stretch an MRI-compatible spring. Rotor angle, gradient angle and output force were recorded as described below.

6.1.1. Experimental method The experiment is shown in Figure 15. The mechanical angle was recorded using a digital video camera (Sony HD, 3.1 MP, 30 fps). The camera was securely mounted 2 m away from the MRI bore entrance and incorporated into its field of view both the motion of the rotor and the motion of the rack. A mirror was used to reflect the line of sight of the (horizontal) rotor to the
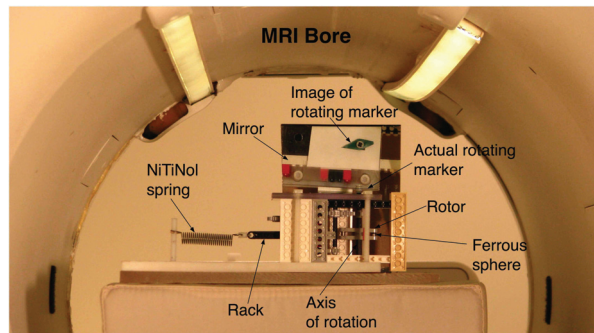
Fig. 15. Experimental design showing actuator at isocenter of MRI bore. Camera located at the viewpoint of the figure records displacement of calibrated spring and rotor rotation.

Fig. 16. Maximum spring force as a function of rotor frequency.

(vertical) plane of the image sensor. The mirror was placed at an angle of $45°$ so that the reflected motor motion does not exhibit any imaging distortion. The mechanical angle was calculated from the reflected image of the rotor using image thresholding, morphological filtering of the resulting binary image to remove noise and speckles, and subsequent selection of the largest connected component. This component corresponded to the rotor, and a line was fit to its contours. The inclination of the line corresponded to the mechanical angle.

The magnetic angle (i.e. the angle of the rotating gradients) was calculated by integrating the constant angular frequency of the rotating magnetic gradients. The elastic load was measured using a calibrated MRI-compatible NiTi spring as shown in Figure 15. As the rotor rotates, the rack retracts, the spring extends and the load applied to the rack increases.

Two sets of experiments were conducted. In the first set of experiments, magnetic gradient frequency was varied between trials in order to determine the dependence of actuator force and stability on frequency. The second set examined repeatability at a single frequency.

6.1.2. Results In the first set of experiments, magnetic gradient frequency was set to values of $f = \{0.4, 0.5, 0.74, 0.83, 0.91, 1.0, 1.25, 1.43, 3\}$ Hz. In each trial, the initial angular speed of the rotor was zero. Figure 16 depicts the maximum output force produced by the actuator at each frequency. The maximum output force is relatively constant up to 1.5 Hz, with a mean value of 520 mN and a standard deviation of 32 mN. As shown by the response at 3 Hz, the rotor is unable to synchronize in open loop with the rotating gradient and, consequently, no output force is produced. This effect is predicted in the undamped case by (34), where $\omega_{max} = 14.86$ rad/sec or 2.4 Hz using the parameter values of Design 1 in Table 1.

To evaluate the variation in response at a particular frequency that could arise from differences in the configuration of the actuator rotor and gears, eight trials were condu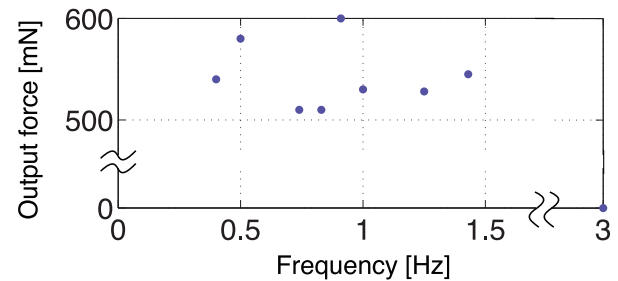cted at a magnetic gradient frequency of 1 Hz. The mean value of the output force was found to be 560 mN with a standard deviation of 27 mN. Thus, for all stable rotor frequencies, the actuator was capable of reliably producing the targeted output force magnitude of 0.5 N.

To evaluate the stability of rotor motion during open-loop control of slip angle, experimental data from a 1 Hz trial was compared with the corresponding simulation results in Section 4. The goal is to validate the theoretical model and demonstrate that simulation can be used to reliably predict the actuator response. The mechanical (rotor) and magnetic angles are depicted in Figure 17. Comparing this figure with Figure 8 reveals that, while similar, the experimental response exhibits several short periods at 46, 63 and 65 s during which the rotor stalls. These are likely due to the use of low-precision, high-friction components that cause perturbations that temporarily drive the rotor trajectory outside the separatrix for stable rotation.

Figure 18 depicts the slip angle for this experiment and Figure 19 provides a detailed view of slip angle leading up to actuator stall at 46 s. Initially, the slip angle oscillates about its slowly increasing equilibrium value, ψ_1, in a manner comparable to Figures 9 and 10. At time $t = 45$ s, however, slip angle temporarily exceeds the maximum stable value of $\pi/2$ and the rotor stalls for one cycle of the magnetic gradient as shown in Figure 20 before commencing to rotate again. Similar behavior was observed at 62 and at 64 s. From 65 to 83 s, mean slip angle increases smoothly until it reaches the critical value of $\pi/2$ at which point the rotor enters instability and stalls permanently. The maximum output force of 564 mN is produced just before instability as shown in Figure 21. The maximum force predicted by simulation in Section 4 was just over 600 mN with the discrepancy likely due to differences in the parameter values used in simulation.

These results demonstrate the capability to perform needle-insertion tasks using open-loop slip angle control. They also demonstrate the capability to produce force magnitudes appropriate for clinical needle insertion. Furthermore, it is interesting to note that this actuator design could produce a force of 2.6 N in the absence of transmission friction ($\eta = 1$). Consequently, output force could easily be substantially increased by optimization of transmission components.
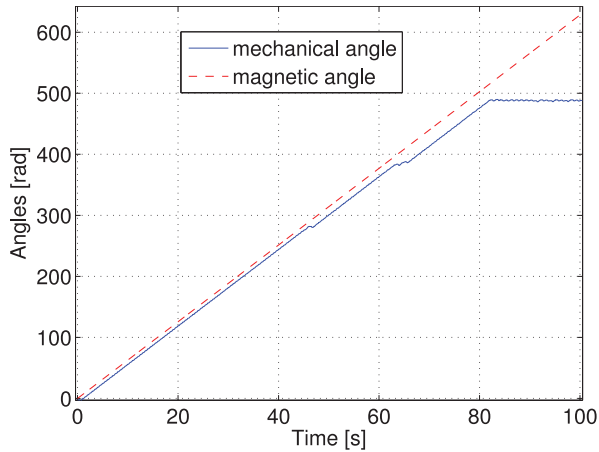
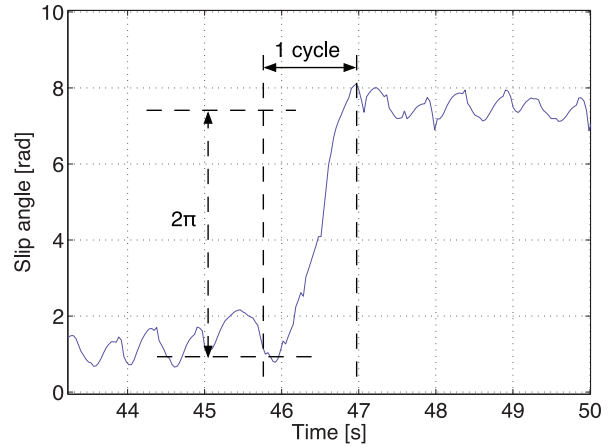**Fig. 17.** Mechanical and magnetic angles as functions of time.

Fig. 20. Slip angle versus time showing rotor stall with mechanical angle falling behind magnetic angle by one revolution (2π).
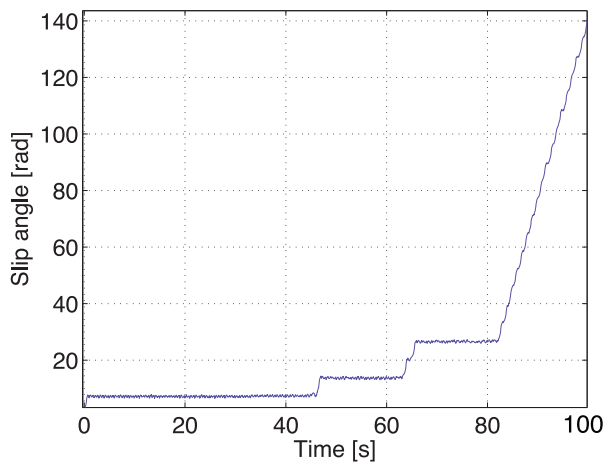

Fig. 18. Slip angle versus time. Note that rotor stalls for one revolution at startup and at times $t = 45, 62, 64$ s. Final stall occurs as $t = 83$ s.
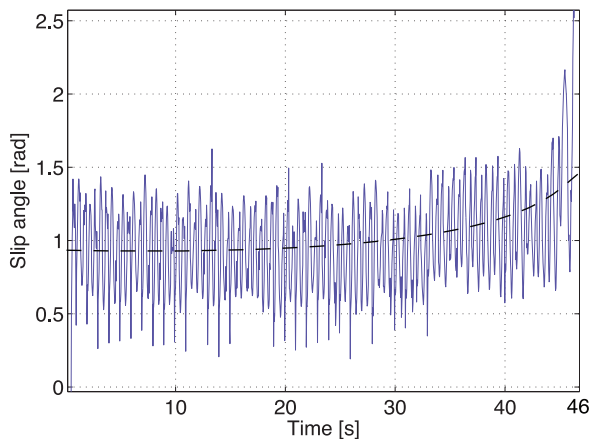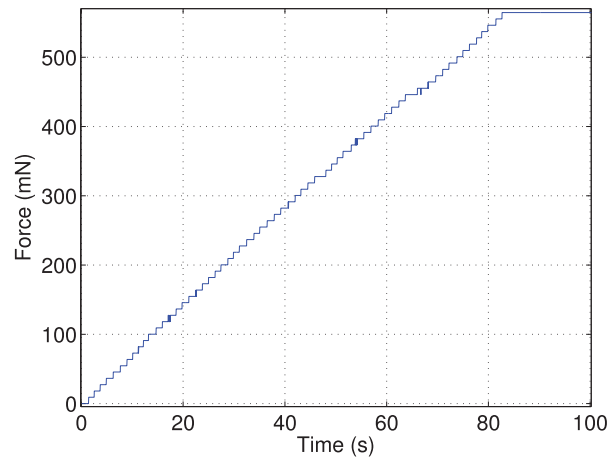

Fig. 21. Spring force versus time.

6.2. Closed-loop needle position control

As shown above, open-loop control of slip angle can enable needle driving into elastic loads. In this section, closed-loop position control is demonstrated using this approach. A fiducial-based method for estimating needle position is first presented. This method is then employed in experiments to drive a needle a specified distance into tissue.

6.2.1. Fiducial-based needle position estimation To evaluate the performance of the localization algorithm of Section 5, single-dimensional projections were captured using a gradient echo of TE = 3 ms, $\alpha = 5°$, field-of-view = 300 mm, bandwidth = ± 64 kHz, matrix = 512 voxels, resulting in a spatial resolution of 580 μm/voxel.

Initially, 10 single-dimensional projections of the tissue (chicken breast) were recorded and an average profile was extracted. Subsequently, a fiducial marker was placed in 5 different locations separated by 20 mm and the algorithm was used to estimate its location (5 repetitions).
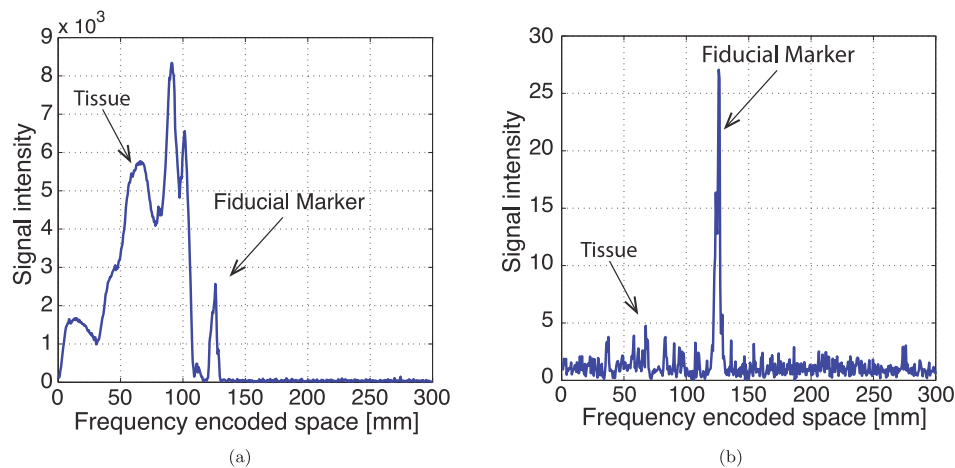

Fig. 19. Slip angle versus time showing increasing mean value up to initial point of stall.

Fig. 22. Fiducial marker signal amplification. (a) Signal intensity versus position in the presence of tissue. (b) Amplified signal intensity versus position obtained applying (42) to (a).

Figure 22(a) and (b) show the single-dimensional projection prior to and after background suppression, respectively. To increase the accuracy of peak detection, a gaussian profile was fit to the maximum intensity values of the marker signal and the central value of the fitted Gaussian was used (Thörmer et al., 2012). The average displacement error over all trials was calculated as -0.65 ± 1.37 mm, which corresponds to 0–5 voxels. This is the expected needle tip localization accuracy and precision for a marker attached to the needle rack.

6.2.2. Position controller For these experiments, the MRI was connected to an image-processing workstation using RTHawk (Santos et al., 2004), resulting in the system network depicted in Figure 23. Needle-insertion experiments into chicken breast were conducted with the tissue covered in plastic wrap to avoid dehydration. A 21-gauge bevel-tip MRI-compatible needle was attached to the actuator rack and a small incision was made through the wrap to allow the needle to directly contact the tissue. To provide the background signal that is required for the tracking algorithm, the single-dimensional tissue signal was captured in the absence of the MRI-powered actuator and the fiducial marker. Subsequently, the actuator was positioned in proximity to the tissue, the needle was aligned with the incision in the plastic wrap, and an initial image volume, as shown in Figure 24(a), was captured using 3-plane gradient echoes with TE = 2.4 ms, TR = 6.7 ms, bandwidth = ± 31.3 kHz, $\alpha = 30°$, field-of-view = 300 mm.

In these experiments, the goal is to advance the tip of the needle by a specified displacement. Under the reasonable assumption that the needle is longitudinally rigid, this is equivalent to translating the fiducial marker by the same distance. Given that each rotation of the rotor corresponds to a needle displacement of 250 μm, the controller

pulse sequence is selected to consist of $N = 5$ propulsion cycles (see Figure 12) corresponding to 1.25 mm of needle displacement per imaging pulse sequence. This displacement is selected to be the largest integer number of cycles that does not exceed the standard deviation of estimator displacement error, 1.37 mm, as measured by the fiducial-based estimator.

The control cycle timing, as labeled in Figure 12, consists of an imaging time, $t_{\text{image}} = 12$ ms, a computational and data transfer time of $t_{\text{proc}} = 200$ ms and an actuation time of $t_{\text{act}} = 5$ s (rotor rotation rate of 1 Hz).

For the trial depicted in Figure 24, the desired displacement was selected as 10 mm. Following the control cycle of Figure 12 and the block diagram of Figure 23, fiducial marker position was first estimated using a tracking pulse sequence and compared with the desired final position. A propulsion sequence was then performed as long as the remaining distance exceeded the propulsion displacement. Final estimated needle displacement for this trial was 9.92 mm.

While eight actuation cycles correspond to exactly 10 mm, it was observed that the controller ran for 12 cycles. This indicates that, similar to Figure 18, open-loop control of slip angle resulted in four cycles in which the rotor stalled. A final 3-plane gradient echo image was captured to evaluate and verify the displacement of the needle and fiducial marker and is shown in Figure 24(b). Needle displacement was confirmed to be 10 mm (1 mm screen resolution) using the scanner console interface by manually selecting the marker centroid before and after displacement. The absence of artifacts in Figure 24 also demonstrates the MR-compatibility of the actuator technology.

7. Conclusion

The MRI-powered actuator technology proposed and demonstrated in this paper offers the potential of enabling
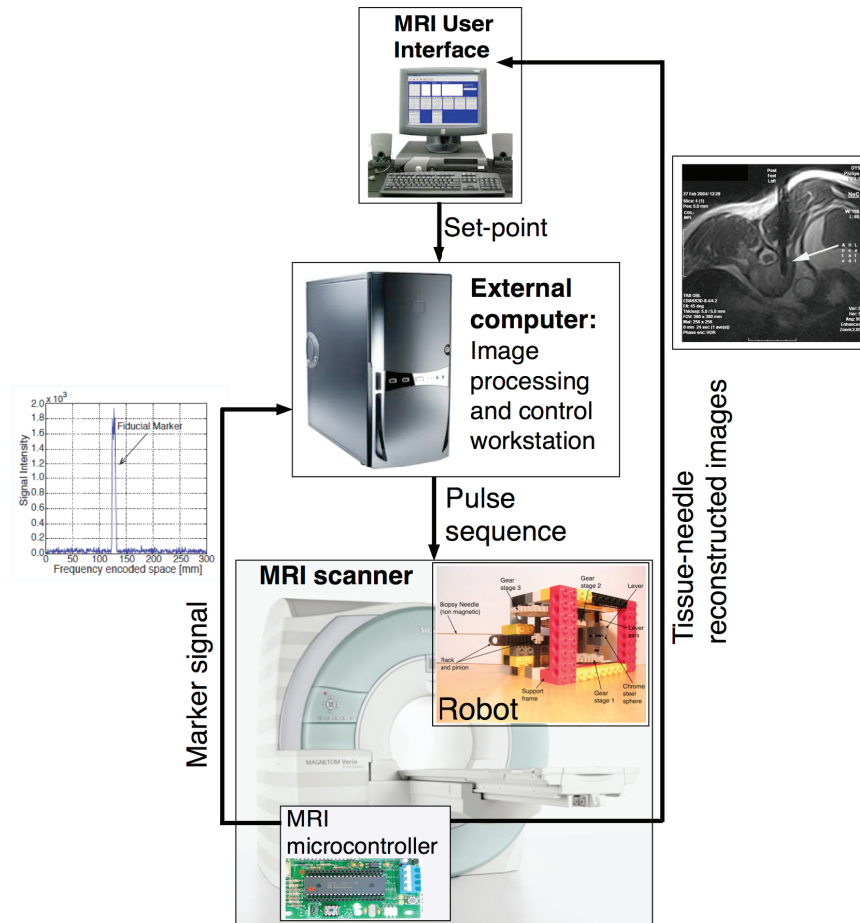
Fig. 23. System network architecture for closed-loop control.

low-cost MRI-guided robotic interventions. Since the actuators can be constructed entirely from plastic and ceramic components encasing one or more standard ball bearings, the overall design is simpler and much less inexpensive than existing MR-compatible robotic actuator technologies. Furthermore, no wires or transmission lines need be run into the scanner bore and, by design, actuator sensing and control is completely integrated with the MR imaging system such that no peripheral devices are required.

Conditions for MRI compatibility are satisfied since all materials except for the ball bearings are non-magnetic and non-conductive. The ball bearings are safely encased in the actuator to prevent their escape and are small enough in volume that they can be located at sufficient distance from the tissue of interest so as to not affect imaging SNR.

The paper provides the fundamental components needed to implement, as well as to further develop, the technology. These include design guidelines to produce application-specific force levels as well as techniques for closed-loop MRI-based actuator state estimation and control. These methods were validated by constructing and testing an actuator designed to produce a maximum force sufficient for porcine spleen insertion. In addition, design specifications appropriate for human prostate needle insertion are also detailed.

There are a number of opportunities to improve this technology through additional research. For example, while open-loop control of slip angle was demonstrated analytically and experimentally to be adequate for needle insertion, there may be applications for which direct control of rotor angle is necessary. Implementing commutation control introduces new challenges and initial work on this topic is reported by Bergeles et al. (2013).

A second topic of interest is to develop actuator designs that incorporate bearings and transmission elements that are both low friction and low cost. If these goals can be met simultaneously, it may be possible to develop single-use actuators for MRI-guided procedures.

As a third topic for future research, many interventional applications require actuating multiple DOFs. A variety of approaches to this problem are currently being investigated. First, full advantage can be taken of the three independent coordinate-direction gradient inputs. In addition, multi-actuator control can be achieved through the use of locking mechanisms as described by Vartholomeos et al. (2011) as well as through the techniques currently being
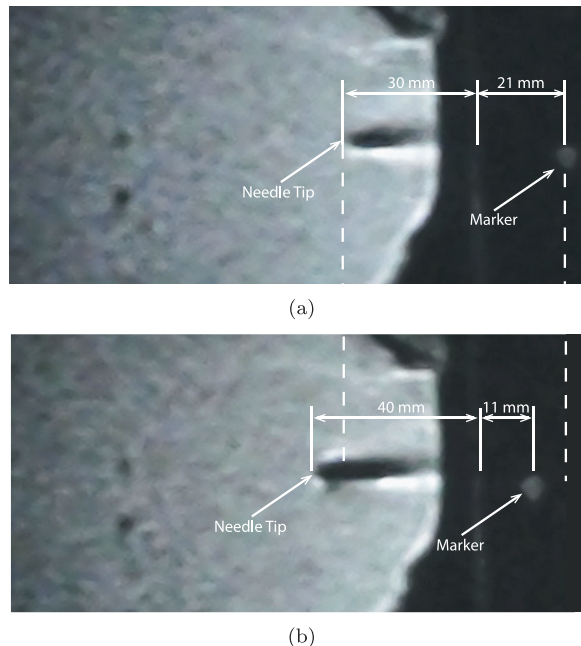
(a)

(b)

Fig. 24. MRI images of position-controlled 10 mm needle displacement into chicken breast: (a) prior to displacement showing needle tip location and fiducial marker; (b) at completion of motion.

developed for the independent control of magnetic milli- and micro-robots (Vartholomeos et al., 2012).

References

Abbott JJ, Ergeneman O, Kummer MP, Hirt AM and Nelson BJ (2007) Modeling magnetic torque and force for controlled manipulation of soft-magnetic bodies. *IEEE Transactions on Robotics* 23(6): 1247–1252.

Arcese L, Fruchard M, Beyeler F, Ferreira A and Nelson BJ (2011) Adaptive backstepping and MEMS force sensor for an MRI-guided microrobot in the vasculature. In: *IEEE International Conference on Robotics and Automation*, pp. 4121–4126.

Barth HV (1973) Ultrasonic driven motor. *IBM Technical Disclosure Bulletin* 2236.

Bergeles C, Qin L, Vartholomeos P and Dupont PE (2012) Tracking and position control of an MRI-powered needle-insertion robot. In: *IEEE International Conference on Engineering in Medicine and Biology*, pp. 928–931.

Bergeles C, Vartholomeos P, Qin L and Dupont PE (2013) Closed-loop commutation control of an MRI-powered robot actuator. In: *IEEE International Conference on Robotics and Automation*, pp. 690–695.

Busse H, Trampel R, Gruünder W, Moche M and Kahn T (2007) Method for automatic localization of MR-visible markers using morphological image processing and conventional pulse sequences: feasibility for image-guided procedures. *Journal of Magnetic Resonance Imaging* 28: 1087–1096.

Chanu A, Felfoul O, Beaudoin G and Martel S (2008) Adapting the clinical MRI software environment for real-time navigation of an endovascular untethered ferromagnetic bead for future endovascular interventions. *Magnetic Resonance in Medicine* 59: 1287–1297.

Chinzei K, Hata N, Jolesz FA and Kikinis R (2000) MR compatible surgical assist robot: system integration and preliminary feasibility study. In: *International Conference on Medical Image Computing and Computer Assisted Intervention*, pp. 921–930.

Felfoul O, Mathieu JB, Beaudoin G and Martel S (2008) In vivo MR-tracking based on magnetic signature selective excitation. *IEEE Transactions on Medical Imaging* 27(1): 28–35.

Fischer GS, Krieger A, Iordachita I, Csoma C, Whitcomb LL and Fichtinger G (2008) MRI compatibility of robot actuation techniques - a comparative study. In: *International Conference on Medical Image Computing and Computer Assisted Intervention*, pp. 509–517.

Giffin A, Shneider M, Chiranjeev KS, Ames TL and Miles RB (2010) Effects of a conducting sphere moving through a gradient magnetic fields. In: *AIAA Aerospace Sciences Meering*, Orlando, FL.

Han BH, Park S and Lee SY (2008) Gradient waveform synthesis for magnetic propulsion using MRI gradient coils. *Physics in Medicine and Biology* 53: 4639.

Lewin JS (1999) Interventional MR imaging: concepts, systems, and applications in neuroradiology. *American Journal of Neuroradiology* 20: 735–748.

Li M, Kapoor A, Mazilu D and Horvath KA (2011) Pneumatic actuated robotic assistant system for aortic valve replacement under MRI guidance. *IEEE Transactions on Biomedical Engineering* 58(2): 443–451.

Martel S, Felfoul O, Mathieu J, et al. (2009) MRI-based medical nanorobotic platform for the control of magnetic nanoparticles and flagellated bacteria for target interventions in human capillaries. *The International Journal of Robotics Research* 28(9): 1169–1182.

Martel S, Mathieu JB, Felfoul O, et al. (2007) Automatic navigation of an untethered device in the artery of a living animal using a conventional clinical magnetic resonance imaging system. *Applied Physics Letters* 90: 114105.

Masamune K, Kobayashi E, Masutani Y, et al. (1995) Development of an MRI-compatible needle insertion manipulator for stereotactic neurosurgery. *Journal of Image Guided Surgery* 1: 242–248.

Maurin B, Barbe L, Bayle B, et al. (2004) *In vivo* study of forces during needle insertions. In: *Perspective in Image-Guided Surgery: Scientific Workshop on Medical Robotics, Navigation and Visualization*, Remagen, Germany, 29 March, pp. 415–422.

McNab JA, Witzel T, Bhat H, et al. (2012) In vivo human brain measurements of axon diameter using 300mT/m maximum

gradient strengths. In: *International Symposium on Magnetic Resonance in Medicine*, p. 20.

Moche M, Trampel R, Kahn T and Busse H (2008) Navigation concepts for MR image-guided interventions. *Journal of Magnetic Resonance Imaging* 27: 276–291.

Patriciu A, Petrisor D, Muntener M, Mazilu D, Schar M and Stoianovici D (2007) Automatic brachytherapy seed placement under MRI guidance. *IEEE Transactions on Biomedical Engineering* 54: 1499–1506.

Podder T, Clark D, Sherman J, et al. (2006) *In vivo* motion and force measurement of surgical needle intervention during prostate brachytherapy. *Medical Physics* 33: 2915.

Qin L, Schmidt EJ, Tse ZTH, et al. (2013) Prospective motion correction using tracking coils. *Magnetic Resonance in Medicine* 69(3): 749–759.

Santos JM, Wright GA and Pauly JM (2004) Flexible real-time magnetic resonance imaging framework. In: *IEEE International Conference on Engineering in Medicine and Biology*, pp. 1048–1051.

Song DY, Burdette EC, Fienne J, et al. (2011) Robotic needle guide for prostate brachytherapy: clinical testing of feasibility and performance. *Brachytherapy* 10: 57–63.

Su H, Cardona DC, Shang W, et al. (2012) A MRI-guided concentric tube continuum robot with piezoelectric actuation: a feasibility study. In: *IEEE International Conference on Robotics and Automation*, pp. 1939–1945.

Thörmer G, Garnov N, Moche M, Haase J, Kahn T and Busse H (2012) Simultaneous 3D localization of multiple MR-visible markers in fully reconstructed MR images: proof-of-concept for subsecond position tracking. *Magnetic Resonance Imaging* 30: 371–381.

Tokuda J, Song SE, Fischer GS, Iordachita I, Seifabadi R, Cho BJ and Fichtinger G (2012) Preclinical evaluation of MRI-compatible pneumatic robot for angulated needle placement in prostate interventions. *Int. J. Computer Assisted Radiology and Surgery* : 1–9.

Tsekos N, Ozcan A and Christoforou E (2005) A prototype manipulator for mr-guided interventions inside standard cylindrical mri scanner. *J. Biomechanical Engineering* (127): 972 –980.

Tsekos NV, Khanicheh A, Christoforou E and Mavroidis C (2007) Magnetic resonance compatible robotic and mechatronic systems for image-guided interventions and rehabilitation: a review study. *Annual Review of Biomedical Engineering* 9: 351–387.

van der Weide R, Bakker CJG and Viergever MA (2001) Localization of intravascular devices with paramagnetic markers in MR images. *IEEE Transactions on Biomedical Engineering* 20(10): 1061–1071.

Vartholomeos P, Akhavan-Sharif MR and Dupont PE (2012) Motion planning for multiple millimeter-scale magnetic capsules in a fluid environment. In: *IEEE International Conference on Robotics and Automation*, pp. 1927–1932.

Vartholomeos P, Qin L and Dupont PE (2011) MRI-powered actuators for robotic interventions. In: *IEEE/RSJ International Conference on Intelligent Robots and Systems*, pp. 4508–4515.

Washio T and Chinzei K (2004) Needle force sensor, robust and sensitive detection of the instant of needle puncture. In: *International Conference on Medical Image Computing and Computer Assisted Intervention*, pp. 113–120.

Zhang K, Krafft AJ, Umathum R, Maier F, Semmler W and Bock M (2010) Real-time MR navigation and localization of an intravascular catheter with ferromagnetic components. *Magnetic Resonance Materials in Physics, Biology and Medicine* 23(3): 153–163.

Appendix: Index to Multimedia Extensions

The multimedia extension page is found at http://www.ijrr.org

Table of Multimedia Extensions

Extension	Type	Description
1	Video	MRI-powered needle insertion into a porcine heart.